

SUBMILLIMETER IMAGING OF T TAURI'S CIRCUMBINARARY DISK AND THE DISCOVERY OF A PROTOSTAR IN HIND'S NEBULA

DAVID A. WEINTRAUB,¹ GÖRAN SANDELL,² TRACY L. HUARD,¹ JOEL H. KASTNER,³
MARIO E. VAN DEN ANCKER,⁴ AND RENS WATERS⁴

Received 1998 May 5; accepted 1999 January 10

ABSTRACT

We have obtained images at 2.2, 450, and 850 μm of the pre-main-sequence binary T Tauri and of Hind's Nebula, which is located less than 1' west of T Tauri. The three maps reveal that the nebulosity around T Tauri is extended, with an FWHM size of several hundred AU in thermal emission and more than 1000 AU in reflected light. Dust clearly connects the circumstellar nebula around T Tauri to the southwestern tip of Hind's Nebula, where we have identified a secondary intensity peak in the submillimeter maps. Calculations of the long-wavelength emissivity demonstrate that the dust emissivity index β is ~ 2 for the large nebula but is ~ 1.2 for the secondary intensity peak. These results for β suggest that we have found a class I protostar 30" southwest of T Tauri and that star formation is more active in the vicinity of T Tauri than previously had been thought. This protostar is detected directly at submillimeter wavelengths; however, polarization mapping at 2.2 μm demonstrates that the disk-shaped dust cloud around the protostar is illuminated externally at short wavelengths, making it similar to the Orion proplyds.

Subject headings: infrared: stars — ISM: individual (NGC 1555) — polarization — reflection nebulae — stars: individual (T Tauri) — stars: pre-main-sequence

1. INTRODUCTION

In the late 1980s, Adams, Lada, & Shu (1988) provided astronomers with a quantitative theory for interpreting the spectral energy distributions (SEDs) of pre-main-sequence stars. In this model, the infrared, far-infrared, and submillimeter continuum excesses observed toward pre-main-sequence stars and protostars were interpreted as the result of photons generated in the stellar photosphere being absorbed and reemitted from dust grains in circumstellar disks. Because of the reprocessing of absorbed stellar photons, the dust grains are heated such that there is an outwardly decreasing radial temperature gradient in the disk. In addition, disks could be self-luminous, generating photons from the release of gravitational potential energy due to accretion. These accretion disks were assumed to have radii of ~ 100 AU. A disk of this size matches our expectations for preplanetary disks—material further from the stars will have extremely long collisional lifetimes so that planets are unlikely to form at these distances. In addition, stellar collapse models appear to generate stellar cores with accretion disks of about this size (Shu et al. 1993).

In generating models of pre-main-sequence stellar disks from SEDs, virtually all far-infrared, submillimeter, and millimeter flux density measurements from the KAO, IRAS,

JCMT, CSO, IRAM, and SEST telescopes⁵ toward T Tauri stars have been assumed to be from unresolved source regions (i.e., sources smaller than $\sim 1''$ for stars at the 140 pc distances of the Taurus and Ophiuchus dark clouds). With the long-wavelength observational data in hand, the Adams et al. (1988) parameterization led to important advances in our understanding of pre-main-sequence disks (e.g., Beckwith & Sargent 1991; Mannings & Emerson 1994). However, there is substantial observational evidence from several directions that suggests that these 100 AU disks are smaller than structures that actually exist around many young stars and that attempts to model these objects should include both compact and extended components.

One line of evidence for large structures comes from direct images of disks now available from the *Hubble Space Telescope*. The radii of silhouetted disks seen in the Orion Nebula (McCaughrean & O'Dell 1996) range from 25 to 500 AU. Because these disks are being photoevaporated, these sizes are lower limits to the disk sizes that once may have existed around these stars. Thus, one would expect that circumstellar disks could be larger in the shielded environments of dark clouds. Padgett et al. (1998) report dark lanes in the circumstellar nebulae around six young stellar objects in Taurus. These dark lanes appear to be circumstellar disks seen in silhouette against bright reflection nebulosity. These disks have radii of 300–750 AU. Also in Taurus, Burrows et al. (1996) discovered a flared disk around HH 30 with a radius of 250 AU.

Additional evidence comes from molecular line imaging of circumstellar disks. In CO emission, the disklike struc-

¹ Department of Physics and Astronomy, Vanderbilt University, P.O. Box 1807 Station B, Nashville, TN 37235; david.a.weintraub@vanderbilt.edu; huard@juggler.phy.vanderbilt.edu.

² National Radio Astronomy Observatory, P.O. Box 2, Green Bank, WV 24944; gsandell@sadira.gb.nrao.edu.

³ MIT Center for Space Research, NE80-6007, Cambridge, MA 02139; jhk@space.mit.edu.

⁴ Astronomical Institute "Anton Pannekoek," University of Amsterdam, Kruislaan 403, NL-1098 SJ Amsterdam, Netherlands; mario@astro.uva.nl; rens@astro.uva.nl.

⁵ KAO = Kuiper Airborne Observatory; IRAS = *Infrared Astronomy Satellite*; JCMT = James Clerk Maxwell Telescope; CSO = Caltech Submillimeter Observatory; IRAM = Institut de Radioastronomie Millimétrique Telescope; SEST = Swedish-ESO Submillimeter Telescope.

ture around GG Tauri extends to 3000 AU (Koerner, Sargent, & Beckwith 1993). In addition, ~ 1000 AU molecular gas disks also are known to exist around HL Tauri (Sargent & Beckwith 1987) and T Tauri (Weintraub, Masson, & Zuckerman 1989). Mannings & Sargent (1997) report that the typical, disklike gas components around Herbig Ae/Be stars and T Tauri stars are resolved with radii as large as 350–400 AU.

Further evidence comes from observations of these sources in the millimeter and submillimeter continuum. GG Tauri has been resolved in continuum emission at 1.4 mm as a $750 \text{ AU} \times 225 \text{ AU}$ source (Koerner et al. 1993) while observations of T Tauri and HL Tauri indicate that these two sources were resolved in the submillimeter continuum using half-power beamwidths (HPBW) of $8''.5$ to $15''$ (Weintraub, Sandell, & Duncan 1989, 1990).

These arguments suggest that dust structures around some pre-main-sequence stars may be resolvable in thermal emission at submillimeter wavelengths with sufficiently sensitive detectors. With the installation of the new submillimeter common user bolometer array (SCUBA) receiver on the JCMT in 1997, it now is possible to observe and map regions around T Tauri stars with greater sensitivity and measure the beam profile more accurately than was possible with earlier generation bolometer detectors such as UKT14. Therefore, it is now possible to determine the spatial distribution of submillimeter emission from dust grains around young stars and whether the dust associated with large molecular gas disks can be detected. In this paper, we report SCUBA observations as well as complementary, near-infrared polarimetric imaging observations of the T Tauri binary system and environment.

2. OBSERVATIONS

The submillimeter and millimeter wavelength observations of T Tauri reported here were obtained with SCUBA during six nights in 1997 and 1998 using SCUBA on the JCMT⁶ on Mauna Kea, Hawaii. SCUBA (Gear & Cunningham 1995) has 37 bolometers in the long- ($850 \mu\text{m}$) and 91 in the short- ($450 \mu\text{m}$) wavelength array separated by approximately two beamwidths in a hexagonal pattern and single pixels available for photometry at longer wavelengths (e.g., at $1300 \mu\text{m}$). The HPBW of SCUBA is $7''.8$ at $450 \mu\text{m}$, $15''$ at $850 \mu\text{m}$, and $\sim 21''$ at $1300 \mu\text{m}$.⁷ Both arrays can be used simultaneously. Except for a single 900 s observation at $1300 \mu\text{m}$, we used the $850 \mu\text{m} + 450 \mu\text{m}$ filter combination in the so-called jiggle-map mode for our observations, where the spacings between the bolometers are filled in by performing a jiggle pattern with the chopping secondary while the secondary is chopping with a frequency of 7.8 Hz. To completely sample both arrays, one needs to sample 64 positions with the array. The time used for each jiggle step was 1 s. Each 64 point jiggle pattern was done in a set of four, 16 point jiggles, each followed by a nod of the telescope into the other beam. We used a $120''$ chop in azimuth, which is marginally sufficient to chop off the

extended emission surrounding T Tauri but short enough to provide good sky cancellation and to not introduce too much coma at $450 \mu\text{m}$. The SCUBA maps were reduced using methods described in the SCUBA mapping cookbook (Sandell 1997).

The dates and a short log of each observing session are given in Table 1. The data were calibrated from maps of Uranus made at the beginning of each night or by bootstrapping Uranus data with maps of AFGL 618 and HL Tau, both of which were used as secondary flux calibrators (Sandell 1994; see footnote 7). The absolute flux densities for these calibrators, as determined from the calibration observations interleaved with our target observations, are known to an accuracy of 15%. In addition, every calibration map made for our program provided a beam map so that we were able to measure the nominal beam profile to an accuracy of 0.1 and determine whether the beam had broadened for any reason at the times of our observations. Consequently, we have very good determinations of the beam size and variations during the course of the observations reported herein. In no case during our program were there any significant variations in the beam size or shape. The submillimeter opacity was determined from sky dips at $850 \mu\text{m}$ and estimates of the 850 and $450 \mu\text{m}$ optical depths based on CSO tau, the sky dip meter located at the CSO, which provides opacity information every 10 minutes at $\lambda = 1300 \mu\text{m}$. Each map was bounded by pointing observations of either 0420–014 or HL Tauri in order to derive an accurate position for the submillimeter position of T Tauri, which we determined to be R.A. = $04^{\text{h}}21^{\text{m}}59^{\text{s}}.4 \pm 1''$ and Decl. = $+19^{\circ}32'06''.9 \pm 1''$ (J2000). This position is within $0''.4$ of the *Hipparcos* (ESA 1997) determined optical position of T Tauri (R.A. = $04^{\text{h}}21^{\text{m}}59^{\text{s}}.42$ and Decl. = $+19^{\circ}32'06''.5$). However, the high but nevertheless limited accuracy of our pointing does not permit us to associate the position of peak emission with either one of the binary components. The $1300 \mu\text{m}$ measurement was obtained by offsetting the telescope directly from HL Tauri to the position noted in Table 2.

We also present $2.2 \mu\text{m}$ (*K*-band) intensity and polarization maps obtained using the near-infrared Cryogenic Optical Bench (COB) mounted at the f15 Cassegrain focus of the Kitt Peak National Observatory 1.3 m telescope⁸ on 1995 January 23 UT. The pixel scale was $0''.93$, as determined astrometrically from images of the OMC1/OMC2 cloud, and the seeing was $1''.9$ (the measured FWHM for field stars in the images of T Tauri and accompanying sky images). These data were obtained while autoguiding and using a cold coronagraph with a diameter of $\sim 3''$. Absolute photometry was measured from unocculted observations of the star 16 Tauri ($K = 5.51$). Three polarimetric image sets were obtained observing the T Tauri field with the coronagraph in front of the $0''.7$ separation T Tauri binary system; a fourth set was obtained in direct observations of an empty field $300''$ west of T Tauri. An identical suite of coronagraphic, polarimetric observations were obtained toward 16 Tauri to determine the level of systemic scattering. Each image set consists of four images obtained at $22''.5$ intervals of a half-wave plate. The individual polarimetric images have effective integration times of 120 s. The final polari-

⁶ The JCMT is operated by the Joint Astronomy Centre, on behalf of the UK Particle Physics and Astronomy Research Council, the Netherlands Organization for Scientific Research, and the Canadian National Research Council.

⁷ Secondary Calibrators for Scuba, linked from <http://www.jach.hawaii.edu/>.

⁸ Kitt Peak National Observatory is part of the National Optical Astronomy Observatories and is operated by Associated Universities for Research in Astronomy, Inc., for the National Science Foundation.

TABLE 1
SCUBA OBSERVATIONS OF T TAURI

UT Date	Calibrators	Number of Integrations ^a	τ_{850}
1997 Sep 7	Uranus, AFGL 618	5	0.28
		5	0.30
1997 Sep 19	AFGL 618, HL Tau	1	0.25
		3	0.26–0.27
		5	0.27
		5	0.27
1997 Nov 30	HL Tau, AFGL 618	5	0.18
		5	0.14
1997 Dec 5 ^b	Uranus, HL Tau, AFGL 618	10	0.11
1997 Dec 17	Uranus, HL Tau, AFGL 618	10	0.11
1998 Mar 6	HL Tau	50 ^c	0.038 ^d

^a Each integration consists of a 64 point jiggle map in the on-beam position followed by a second 64 point jiggle map in the off-beam position.

^b Extremely high sky noise in these integrations.

^c The 1.3 mm observation consists of 50 on-off pairs, 9 s per position, for a total integration time of 900 s.

^d $\tau_{1.3 \text{ mm}}$.

metric images at each interval position of the half-wave plate are obtained by co-adding images from the three polarimetric image suites (360 s effective integration times), and a total intensity map is obtained by co-adding and averaging the four, final polarimetric images. The method for calculating the degree and position angles of polarization from the individual COB images is described by Huard, Weintraub, & Kastner (1997).

3. RESULTS

3.1. *T Tauri's Submillimeter Nebula*

These new 450 μm (Fig. 1a) and 850 μm (Fig. 1b) maps obtained with SCUBA confirm that T Tauri is resolved by the JCMT beam at submillimeter wavelengths, with FWHMs of $9''.6 \times 8''.6$ at 450 μm and $17''.4 \times 15''.5$ at 850 μm . In comparison, over the same time period during which these observations of T Tauri were obtained, Sandell⁷ reports that sources such as CRL 618 (which one might expect to be extended) and HL Tauri are either unresolved or are far more compact than T Tauri. Sandell reports FWHMs of $7''.9\text{--}8''.1$ at 450 μm and $14''.7$ at 850 μm for CRL 618, compared with HPBW's of $8''.1\text{--}8''.3$ and $14''.8$ for Uranus. Thus, there is no doubt that T Tauri is resolved in the JCMT maps.

While no submillimeter emission appears to the north or east of T Tauri, the maps reveal a low-luminosity nebula that extends to the south and southwest of T Tauri. The low surface brightness nebula connects T Tauri to Hind's Nebula, encompasses all of Hind's Nebula, and extends out to distances of more than an arcminute from T Tauri. In the vicinity of Hind's Nebula, and within the limited resolution of the submillimeter beams, the long-wavelength emission roughly follows the overall north-south crescent shape of the nebula seen in optical and near-infrared images (see Fig. 2a; also Bührke, Brugel, & Mundt 1986; Hodapp 1994).

While most of Hind's Nebula is featureless in these images, the Nebula does have an intensity peak $\sim 30''$ southwest of T Tauri. As we will discuss in § 3.2, this intensity peak also is seen in 2.2 μm images. Within the relative accuracies of the differing beam and pixel sizes, the intensity peaks in Hind's Nebula at 2.2, 450, and 850 μm are coincident (Table 2; fifth column) at a position $25''$ west and $17''$ south of T Tauri. We will demonstrate (§ 4.2) that this intensity peak is a deeply embedded protostar and thus, for the rest of this paper, shall refer to this southwest intensity peak as Hind's protostar.

These submillimeter maps show no indication of the presence of a second source $\sim 12''$ south of T Tauri, as seen at

TABLE 2
SCUBA OBSERVATIONS OF T TAURI AND HIND'S NEBULA

Source	λ (μm)	Peak Intensity ^a (Jy beam ⁻¹)	Background Intensity ^b (Jy beam ⁻¹)	Offset from T Tauri (R.A., Decl.)	Measured Size (FWHM) (arcsec)	Deconvolved Size (FWHM) (arcsec)	Position Angle (deg)
T Tauri	850	0.64	0.15	...	17.4×15.5	8.8×3.9	+13
	450	2.38	0.57	...	9.6×8.6	5.6×3.6	+31
	2	5.2×6.9	5.2×6.9	+0
Hind's protostar	1300	0.027	0.051	-25, -17
	850	0.098	0.178	-22.6, -14.8	21.6×18.8	15.5×11.3	-56
	450	0.22	0.63	-25.3, -16.9	15.4×10.6	13.2×7.2	-8.5
	2	4.8	0.103	-25.2, -17.0	11.4×5.4	11.4×5.4	-35

NOTE.—Units of right ascension and declination are arcseconds.

^a At 2 μm , the given value is the integrated flux density (mJy) from Hind's protostar, equal to a magnitude of $K = 12.86$.

^b At 2 μm , the given value is the surface flux density (mJy arcsec⁻²) from Hind's Nebula, equal to $17''.00 \text{ arcsec}^{-2}$ at the K band.

T Tau

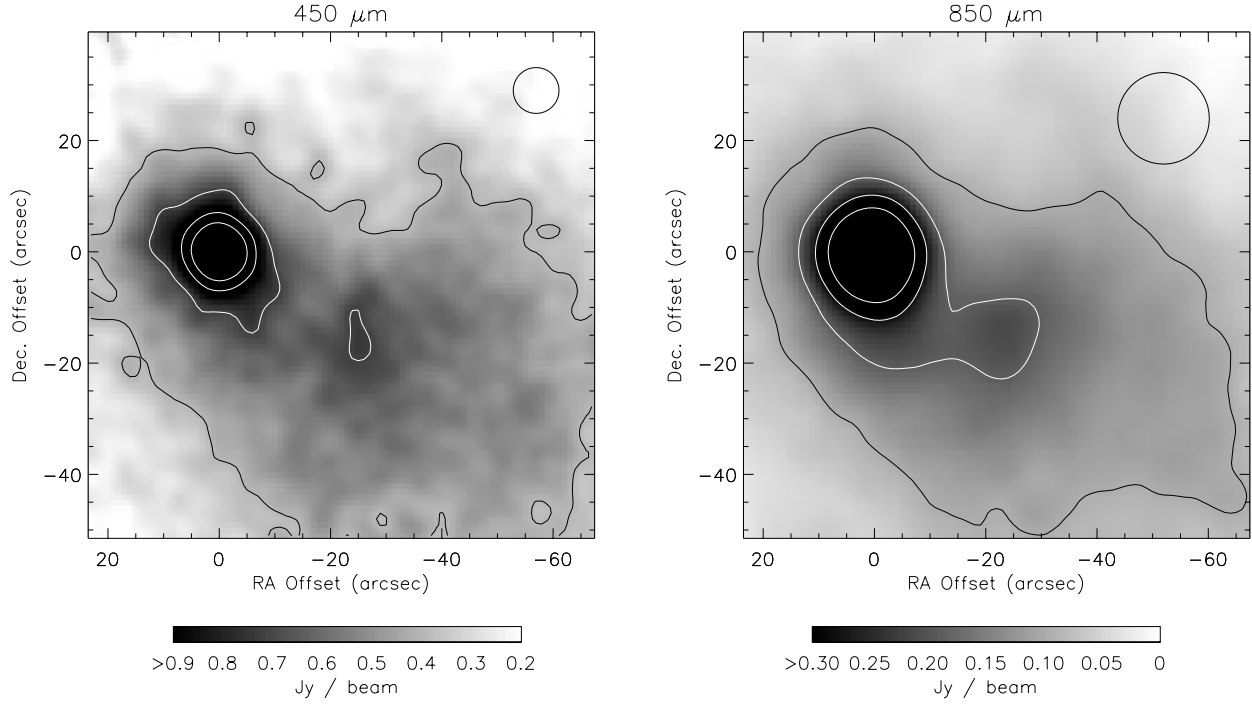


FIG. 1.—(a) SCUBA map of T Tauri at $450\ \mu\text{m}$. Contours are drawn at 15%, 30%, 45%, and 60% of the peak intensity. Note the extended nebula around T Tauri itself (at offset position $0'', 0''$), the nebulosity connecting T Tauri to Hind’s Nebula along P.A. $\sim 225^\circ$, and the bright, resolved source, Hind’s protostar, located at the southern tip of Hind’s Nebula, about $30''$ from T Tauri (at offset position $-25'', -17''$). The beam, shown in the top right corner, has an HPBW of $8''.5$. (b) SCUBA map of T Tauri at $850\ \mu\text{m}$. Contours are drawn at 15%, 30%, 45%, and 60% of the peak intensity. Both T Tauri and Hind’s protostar are resolved, even in the large beam maps at this wavelength. The beam, shown in the top right-hand corner, has an HPBW of $15''$.

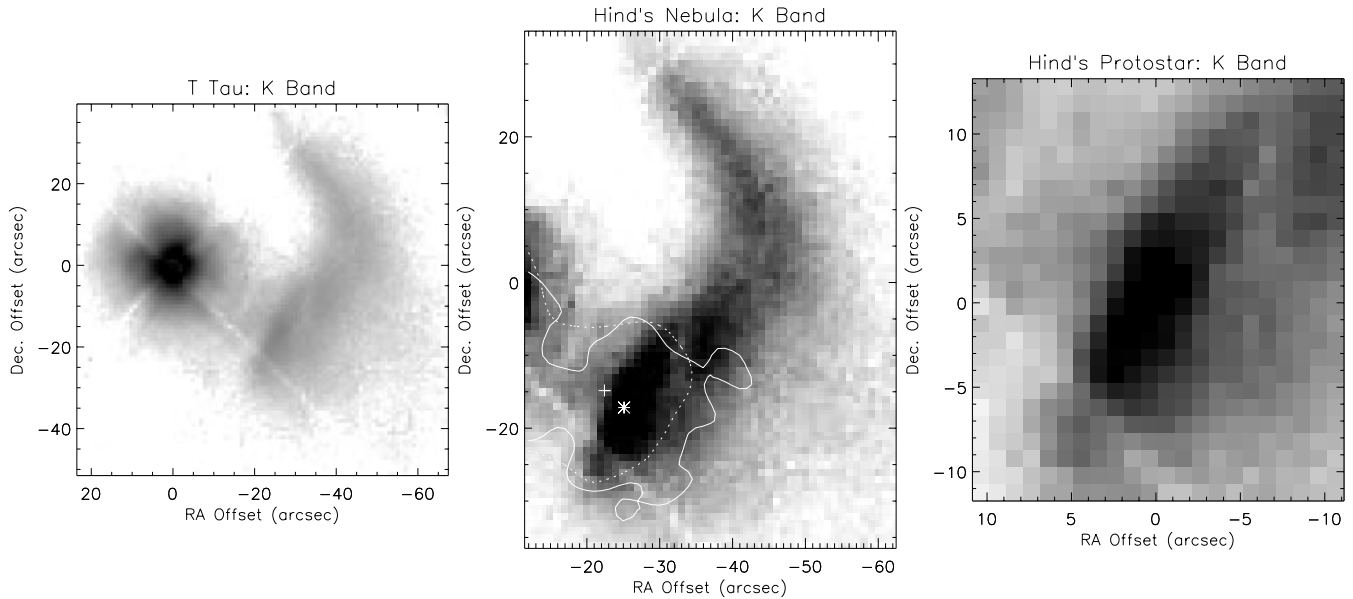


FIG. 2.—(a) K-band, coronagraphic image of T Tauri and Hind’s Nebula. T Tauri is located at offset position $(0'', 0'')$. The straight, almost white lines that extend from T Tauri toward position angles 45° , 135° , 225° , and 315° (seen also in Figs. 2b and 2c) are the positions of the coronagraphic spider wires. Gray-scale intensities have been adjusted to show detail in the nebula around T Tauri. (b) Close-up K-band image of Hind’s Nebula. Again, T Tauri is located at offset position $(0'', 0'')$, slightly out of this field of view. Gray-scale intensities have been adjusted to show detail in Hind’s Nebula. The solid and dashed contour lines are overlays of the $450\ \mu\text{m}$ and $850\ \mu\text{m}$ images, respectively, drawn at 80% of the local intensity peak at the respective wavelengths. The star and plus symbols mark the positions of the local intensity peaks in the $450\ \mu\text{m}$ and $850\ \mu\text{m}$ images, respectively, and indicate the approximate location of Hind’s protostar. (c) Close-up of Hind’s protostar at K band (located at offset position $0'', 0''$). Gray-scale intensities have been adjusted to show detail in the immediate vicinity of this source. Note that the bright, straight line at P.A. 45° , in the lower left-hand portion of the figure, is from the wire holding the coronagraph (that occults T Tauri in Fig. 2a).

the 4σ level in the 2.7 mm map (but not the 3.4 mm map) of T Tauri presented by Hogerheijde et al. (1997a). This second source has a reported peak brightness of ~ 12 mJy at 2.7 mm; assuming it is a thermal emission source, we would expect such a source to be easily detectable (with a flux density of several hundred mJy at $850\ \mu\text{m}$) in our maps, but we see no hint of such a source, which suggests that it is not real.

For the regions around T Tauri and Hind's protostar, we have fitted two-dimensional Gaussians to the peaks to determine the positions and FWHM of the peaks as well as the peak and background intensities (Table 2). In these maps, each Gaussian peak stands on top of a plateau of nearly uniform emission. The uniform background intensity includes contributions from the error lobes of the intensity peaks in addition to emission from the extended nebula.

At $450\ \mu\text{m}$, the peak flux from T Tauri is $2.23\ \text{Jy beam}^{-1}$ above a background level of $0.72\ \text{Jy beam}^{-1}$. At this wavelength, the error lobe contribution from the peak is about 6.5% of the peak (i.e., $0.15\ \text{Jy}$ for T Tauri); thus, the error lobe corrected peak flux is $2.38\ \text{Jy beam}^{-1}$ superposed on an extended cloud component of $0.57\ \text{Jy beam}^{-1}$. Similar measurements of the peak and background levels around Hind's protostar indicate that, after correcting for the error lobes, the peak and background levels are 0.22 and $0.63\ \text{Jy beam}^{-1}$, respectively, at $450\ \mu\text{m}$. The integrated $450\ \mu\text{m}$ flux density across the entire map is $28.3\ \text{Jy}$. Note that the error in our measurements of the flux densities is dominated by the uncertainty in the absolute calibration, not by statistical uncertainties.

At $850\ \mu\text{m}$, the peak flux from T Tauri is $0.64\ \text{Jy beam}^{-1}$ on a background level of $0.15\ \text{Jy beam}^{-1}$. At this wavelength, the error lobe contribution is less than 1% of the peak so the error lobe corrected peak and background levels are almost indistinguishable from the uncorrected levels. For Hind's protostar, the error beam corrected, $850\ \mu\text{m}$ flux densities are $0.098\ \text{Jy beam}^{-1}$ for the peak and $0.178\ \text{Jy beam}^{-1}$ for the background. The integrated $850\ \mu\text{m}$ flux density across the entire map is $3.34\ \text{Jy}$.

From the single pointed observation at $1300\ \mu\text{m}$, we determined that the long-wavelength flux density in the vicinity of Hind's protostar is $0.078\ \text{Jy}$. We can be certain that the observed total flux density at $1300\ \mu\text{m}$ is the sum of contributions from Hind's protostar and the background. Given that the ratio of the flux from Hind's protostar to the total flux (source plus background) is 0.26 at $450\ \mu\text{m}$ and 0.36 at $850\ \mu\text{m}$, we roughly approximate that the protostar produces $\sim 35\%$ ($0.027\ \text{Jy beam}^{-1}$) and the background 65% ($0.051\ \text{Jy beam}^{-1}$) of the total flux at $1300\ \mu\text{m}$.

The deconvolved source sizes can be found from the measured FWHMs of the sources (Ω_{FWHM}) and the measured HPBW of the telescope (Ω_{beam}) at each wavelength. From Ω_{FWHM} of the peaks around T Tauri and Hind's protostar, it is clear that both sources are broader than the beam size. The deconvolved nebular sizes (Ω_s), given in Table 2, are obtained from the formula

$$\Omega_s = (\Omega_{\text{FWHM}}^2 - \Omega_{\text{beam}}^2)^{0.5}.$$

For T Tauri at $450\ \mu\text{m}$, Ω_{FWHM} of the cold, dust source is $9''.6 \times 8''.6$ and $=5''.6 \times 3''.6$ (Table 2), or $\sim 780\ \text{AU} \times 500\ \text{AU}$, with the major axis oriented at P.A. 31° . At $850\ \mu\text{m}$, we find $\Omega_{\text{FWHM}} = 17''.4 \times 15''.5$ and thus $\Omega_s = 8''.8 \times 3''.9$ at P.A. 13° . At both wavelengths, T Tauri is *clearly resolved*

beyond any errors in the measurement of the beam size in both dimensions. In addition, the P.A. of the major axis agrees quite well at the two wavelengths, with a mean value of 22° . This result also agrees extremely well with the major axis of 19° found by Akeson, Koerner, & Jensen (1998) for the $0''.45 \times 0''.32$ compact source found around T Tauri N. Because the extended component shares the same orientation as the compact source around T Tauri N, it is quite possible that the source resolved by the JCMT beam is similarly associated with T Tauri N or a larger circumbinary disk too faint to be detected with the sensitivities of current millimeter-wavelength, aperture synthesis telescopes. Whether this structure is an extension of the T Tauri N disk or a circumbinary disk, it clearly would obscure our view of T Tauri S, thus explaining why T Tauri S is so highly reddened. Thus, although it might be debatable whether the extended emission we see is the outer portion of the T Tauri N disk, a circumbinary disk, or a "pseudodisk" (Galli & Shu 1993), it clearly has a disklike morphology and not that of a "classical" envelope.

The dusty nebula around Hind's protostar is larger and colder than the dusty structure around T Tauri, with a deconvolved size of $\sim 15''.5 \times 11''.3$ ($\sim 2100\ \text{AU} \times 1500\ \text{AU}$) at $850\ \mu\text{m}$ and $\sim 12''.8 \times 6''.3$ at $450\ \mu\text{m}$.

Although the dust source around a given star can have only one physical size, several reasons exist that explain why we are likely to obtain smaller apparent source sizes at the shorter wavelength. First, at the shorter wavelength, we are dominated by emission from hotter dust grains, which should naturally lead to our measuring a slightly smaller source size. In addition, SCUBA is almost 8 times more sensitive at $850\ \mu\text{m}$ than at $450\ \mu\text{m}$; hence, unless a source has an effective slope (α) to the SED that is greater than ~ 3.3 , the source will be easier to detect at $850\ \mu\text{m}$. This is certainly the case for the dust associated with T Tauri, where $\alpha < 3$. Third, since the flux from the more extended portions of the nebula is at a low level above a uniform background of cloud emission, the circumstellar nebula becomes even harder to detect (because it is less bright compared with the background) in the short-wavelength measurements.

Related to this issue of differing source sizes at different wavelengths and with different beam sizes is the discrepancy between disk sizes as measured in thermal emission versus these sizes as detected in molecular gas. Mannings & Sargent (1997) provide a summary comparison of source sizes for both Herbig Ae/Be stars and T Tauri stars. For the former, they find that the typical dust component is unresolved and smaller than $300\ \text{AU}$ in radius while the typical gas component is resolved and has a radius of 250 – $400\ \text{AU}$. For the T Tauri stars, the unresolved dust component is smaller than $180\ \text{AU}$ in radius while the typical gas component is 110 – $350\ \text{AU}$. GG Tauri has a disk radius of $375\ \text{AU}$ in $1.4\ \text{mm}$ continuum emission yet has a CO disk radius of $3000\ \text{AU}$ (Koerner et al. 1993).

How are we to make sense of these results? Clearly, where there is gas there almost certainly is dust and so the dusty, disklike structures around these stars must be as large as the gas disks. The dust, the detection of which depends on both the temperature and surface density distributions, may be too cold or rarefied to enable detection with past or even current instrument sensitivities, especially aperture synthesis telescopes, which tend to filter out faint extended emission. Single-dish telescopes, like the

JCMT, are definitely more sensitive to spatially extended emission.

The combination of thermal imaging, molecular line imaging, and scattered light imaging (Weintraub et al. 1992 and § 3.4) provides strong evidence that a disklike gas and dust structure of at least several hundred AU in extent exists around the central T Tauri binary. We next attempt to determine the relative contributions to the measured JCMT flux density of the unresolved and resolved components.

3.2. A Two-Component Emission Source for T Tauri

In analyzing the submillimeter spectrum of T Tauri, the nonthermal emission component cannot be ignored. Since the time that Spencer & Schwartz (1974) discovered that T Tauri is a radio source, this star has been observed at radio frequencies several times (Schwartz & Spencer 1979; Spencer & Schwartz 1974; Cohen, Bieging, & Schwartz 1982; Bieging, Cohen, & Schwarz 1984; Skinner & Brown 1996; Ray et al. 1997; Koerner et al. 1999). A comparison of the 6 cm observations of the T Tauri system spanning several years shows no discernible variability in the centimeter regime flux densities. However, Skinner & Brown report variations of 50% over 3 days in the 3.6 cm flux density of T Tauri S.

Schwartz, Simon, & Campbell (1986) resolved the T Tauri system and showed that the centimeter emission arises from three components, T Tauri S, which is much brighter than T Tauri N, T Tauri N, and a bridge connecting these two stars. These authors assigned a spectral slope of $\alpha = 0.44$ to the southern component ($F_{2\text{ cm}} = 8.1$ mJy, $F_{6\text{ cm}} = 5.0$ mJy) and $\alpha = 1.0$ to the northern component ($F_{2\text{ cm}} = 2.2$ mJy, $F_{6\text{ cm}} = 0.7$ mJy).

Koerner et al. (1996, 1999) report that the radio emission spectrum from T Tauri S extends from 3.4 to 0.7 mm with $\alpha = 1.2$, demonstrating the presence of a strong component of free-free emission from T Tauri S to wavelengths as short as 7 mm. They also detect emission from T Tauri N at 7 mm; however, they report a steeper slope for the spectrum of T Tauri N and suggest that thermal emission may be a more important contributor to the total emission of T Tauri N than to T Tauri S at 7 mm.

Skinner & Brown (1996) report that the spectral index of T Tauri S may be as small as -0.50 or as large as $+0.44$; they conclude that it is likely variable but is consistent with being largely flat, with a flux density close to 5 mJy from 2 to 6 cm. For T Tauri N, the spectral index is also poorly constrained and may range from -0.35 to $+0.65$. These authors conclude that the radio flux from T Tauri N is likely due to free-free emission from an ionized stellar wind, for which a spectral index of 0.60 is reasonable (Wright & Barlow 1975; Panagia & Felli 1975). For T Tauri S, they attribute the radio emission to nonthermal gyrosynchrotron emission, for which we can assume, on average, a negative spectral index or zero.

Given this, we examine what is known about emission from T Tauri at 2.78 mm (108 GHz), where Akeson et al. (1998) have made high-resolution interferometric observations. First, we estimate that the total nonthermal emission is 11 mJy at 2.78 mm: T Tauri S contributes ~ 5 mJy at 2.8 mm (i.e., unchanged from centimeter wavelengths) and T Tauri N contributes ~ 6 mJy (i.e., assuming $F = 1.2$ mJy at 3.6 cm and $\alpha = 0.6$). Akeson et al. detected 50 ± 6 mJy of emission at 2.78 mm, which they found centered on T Tauri

N; they assign all of this emission to T Tauri N and assign less than 9 mJy to T Tauri S. The Akeson et al. result is consistent with large-aperture observations at comparable wavelengths: Momose et al. (1996) detected 48 ± 7 mJy of unresolved emission at 2.73 mm (HPBW $17''$), while Ohashi et al. (1996) found 56 ± 10 mJy at 3 mm in an unresolved region smaller than 550×420 AU. Hogerheijde et al. (1997b) found 39.1 ± 4.2 mJy at 2.7 mm in a $3''$ beam. At this wavelength, they report having resolved T Tauri with an FWHM of $9'' \times 7''$. At a slightly longer wavelength, Hogerheijde et al. (1997a) reported 45.6 ± 5.5 mJy in a $6''$ beam at 3.4 mm. Thus, this full complement of observations suggests, within the errors, that most or all of the 2.7 mm flux density comes from the compact source around T Tauri N seen by Akeson et al. Of the 50 mJy total emission measured by Akeson et al., we conclude that 45 ± 6 mJy is thermal emission.

In the only other high-resolution interferometric maps of T Tauri, Hogerheijde et al. (1997b) report a flux of 397 ± 35 mJy at 1.1 mm (267 GHz) from an unresolved source that they associate with T Tauri N. Our extrapolation of the radio emission from T Tauri N suggests that 9 mJy of this total is free-free, leaving 388 ± 35 mJy as thermal emission.

We now use this information to determine the flux associated with the resolved structure as observed in the SCUBA maps. The thermal emission from T Tauri N is consistent with a spectral index of $\alpha = 2.38 \pm 0.24$, where the error is based on the 1σ error placed on both the 267 and 108 GHz observations. Assuming that the 2.78 mm flux density is in the range of 39–51 mJy, one predicts 570–1000 mJy of flux from the compact source at $850\ \mu\text{m}$. Of course, the high end of this range is inconsistent with our measurement of a peak flux of 630 mJy (we have subtracted 10 mJy of nonthermal emission from the $850\ \mu\text{m}$ peak flux per beam), so a better constraint becomes 570–630 mJy for the compact source. Thus, it would appear that the flux per beam from the extended component at $850\ \mu\text{m}$ is restricted to the range 0–60 mJy.

The total flux from a resolved source is found by multiplying the peak thermal continuum flux per beam by a factor, A_λ , where

$$A_\lambda = \left[1.0 + \left(\frac{\Omega_{\text{FWHM}_1}}{\Omega_{\text{beam}}} \right)^2 \right]^{0.5} \times \left[1.0 + \left(\frac{\Omega_{\text{FWHM}_2}}{\Omega_{\text{beam}}} \right)^2 \right]^{0.5}$$

and Ω_{FWHM_1} and Ω_{FWHM_2} are the deconvolved major and minor axis sizes of the submillimeter source. For T Tauri, $A_{450} = 1.69$ and $A_{850} = 1.20$, where we have used the size as measured at $850\ \mu\text{m}$, under the assumption that our observations were more sensitive to the coolest dust in the $850\ \mu\text{m}$ rather than the $450\ \mu\text{m}$ data. Next, in order to calculate the total flux from T Tauri at these wavelengths, we must determine what fraction of the 450 and $850\ \mu\text{m}$ flux densities that we observed are from thermal versus nonthermal emission.

Given our scaling factor of 1.20 to from flux per beam to total flux, this gives a range for the total flux of 0–72 mJy from the resolved structure around T Tauri. One could conclude from this analysis that all the submillimeter flux is associated with the compact source seen by Akeson et al. (1998). However, that conclusion is inconsistent with our observations in which T Tauri N is clearly resolved. Thus, while we cannot attribute an absolute flux level to the

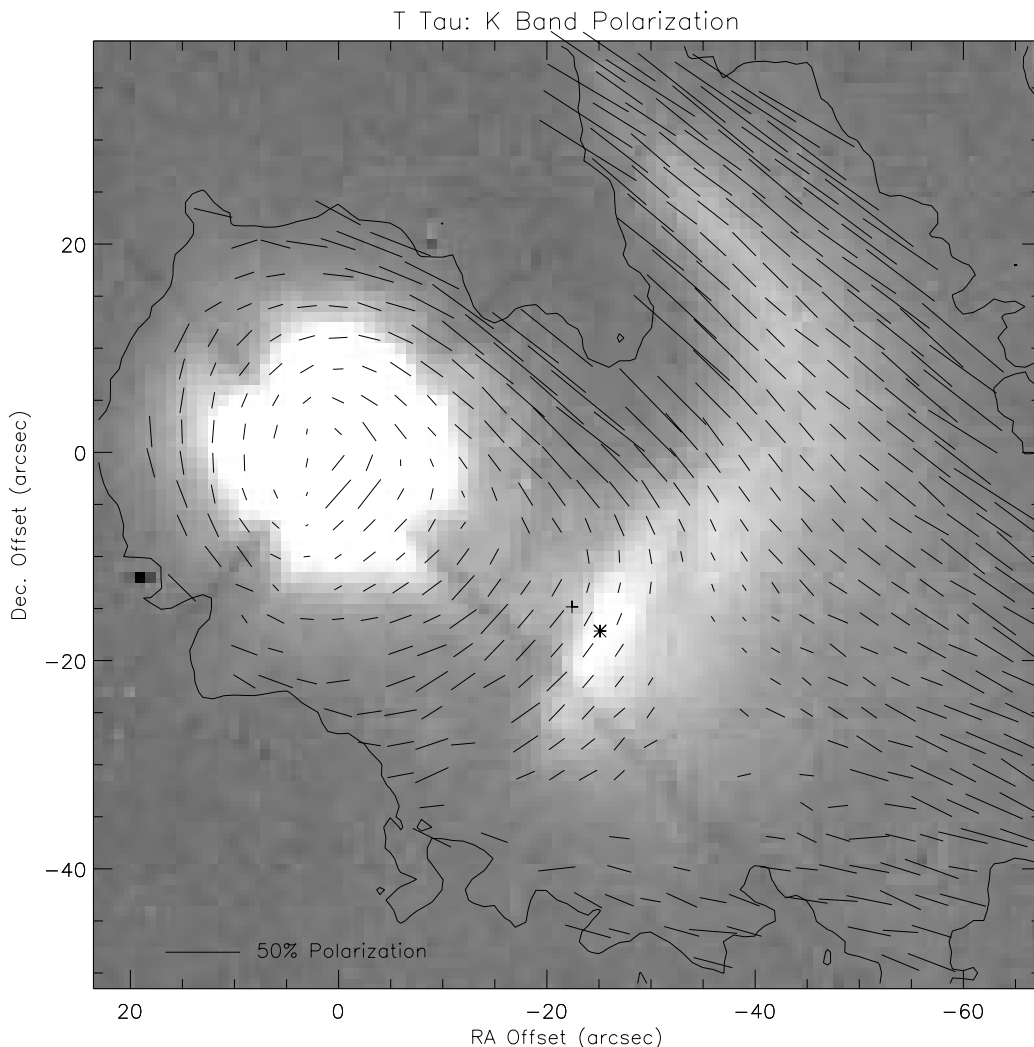


FIG. 3.—K-band polarization vectors overlain on K-band intensity image. The length of the vectors is proportional to the percent polarization. A 50% fiducial vector is shown in the lower left-hand corner. Vectors are plotted if the signal-to-noise ratio in a given pixel is greater than 3 and if the percent polarization is greater than 3 times the error in that measurement. The error in position angles of most vectors is known to within 10° . The single contour indicates the 3σ intensity limit above the sky and background level. The star and plus symbols are the same as in Fig. 2b.

resolved component, we conclude that such a source region exists and contributes up to 72 mJy of total emission, equivalent to up to $\sim 13\%$ of the flux from the compact source.

3.3. Total Flux Density from Hind's Protostar and the Background Cloud

For Hind's protostar, $A_{450} = 3.62$, $A_{850} = 1.78$, and $A_{1300} = 1.41$. Thus, for Hind's protostar, we find 0.80, 0.17, and 0.038 Jy at 450, 850, and 1300 μm , respectively. Having found the total flux density for Hind's protostar we can subtract the total flux contributed by the two sources (totals of 3.2 Jy at 450 μm and 0.81 Jy at 850 μm) from the measured total flux densities in the map to obtain the total integrated flux from the nebula itself, 25.1 Jy at 450 μm and 2.53 Jy at 850 μm .

3.4. Two Micron Imaging and Polarimetry

The 2.2 μm coronagraphic, polarimetric images reveal an extended reflection nebula around the T Tauri binary (Fig.

2a) and faint nebulosity all along the crescent shape of Hind's Nebula (Fig. 2b). The dust bridge that is seen to connect T Tauri to Hind's Nebula at 450 and 850 μm also is seen in the K-band image. The image is very similar to 6900 \AA continuum CCD images of the region (Bührke et al. 1986) except that the dust bridge is more evident in the deeper, coronagraphic image presented here.

In contrast, coronagraphic, polarimetric observations of 16 Tau (not shown) made with the identical observing setup and protocol as the observations of T Tauri are completely void of flux. The source 16 Tauri is presumed to be a point source and is almost identical in K-band magnitude to T Tauri. Thus, the observations of 16 Tauri demonstrate the *complete* absence of systemic scattered light in the 1.3 m + COB + coronagraph polarimetric imaging system for a point source as bright as T Tauri. Therefore, the large bright region at the center of the coronagraphic image of T Tauri is from a large, 2.2 μm reflection nebula immediately around T Tauri.

This K-band reflection nebula extends more than $15''$

radially outward in all directions from T Tauri. This result, which confirms earlier coronagraphic work (Weintraub et al. 1992) that showed a circularly symmetric reflection nebula, illuminated by T Tauri and/or its companion out to at least $10''$ from the central binary, reveals that the dust grains detected in thermal emission in the submillimeter also are seen in reflected light in the near-infrared. A Gaussian fit to the K -band nebula around T Tauri yields an FWHM size of $5''.2 \times 6''.9$ (R.A. \times decl.).

In the immediate vicinity of Hind's protostar, the images at K band show an elliptically shaped nebula (Fig. 2c). This nebula has an FWHM of $\sim 11''.4 \times 5''.4$, at a P.A. of about -35° , which is remarkably similar in size and orientation to that seen in the submillimeter. The integrated K -band luminosity for this object is $K = 12.86$, while the nearly uniform surface brightness of Hind's Nebula is $K = 17.00$ mag arcsec $^{-2}$. The highly elliptical shape, as seen in projection, is much longer along its major axis (800 AU in "radius") and thicker along its minor axis (380 AU in "height") than expected for a circumstellar disk but is very similar in size to the disk around HH 30 (Burrows et al. 1996) and several of the Orion proplyds, e.g., Orion 114–426 (McCaughrean et al. 1998).

The polarization vector map (Fig. 3), in particular the centrosymmetric vector pattern immediately around T Tauri as seen already by Weintraub et al. (1992) for a slightly smaller region, demonstrates that at $2.2 \mu\text{m}$ this dusty region is seen entirely in reflected light whose source is one or both of the stars that make up the T Tauri binary system. Similarly, the polarization pattern seen in the material connecting the nebula immediately around T Tauri to Hind's Nebula indicates that this part of the nebula is seen entirely in scattered light at $2.2 \mu\text{m}$. The polarization pattern in between T Tauri and Hind's protostar appears as an elliptically symmetric extension of the circular pattern centered on T Tauri, with the ellipse stretching outward toward P.A. 225° to just beyond the position of Hind's protostar.

The polarization signature of the nebulosity directly associated with Hind's protostar also shows a centrosymmetric pattern oriented toward T Tauri. The polarization map demonstrates that in the near-infrared, the dust in the vicinity of Hind's protostar is illuminated externally by T Tauri and is not direct (or reprocessed) emission from Hind's protostar. This result also demonstrates that T Tauri, Hind's Nebula, and Hind's protostar are in close physical proximity, i.e., not merely seen near each other in projection along the line of sight. Thus, the polarization map strongly indicates that any optical or near-infrared emission from the deeply embedded protostar is absorbed and reprocessed before emerging from this dense cocoon and that the protostar can be detected directly only at much longer wavelengths.

The polarization measured toward the fainter parts of Hind's Nebula is more difficult to interpret. The linear pattern of polarization position angles in the outskirts of the nebula, where the position angles are oriented perpendicular to the line of sight from the midpoint between T Tauri and Hind's protostar, is suggestive of a high degree of secondary scattering of a combination of reflected light from the T Tauri nebula and from the envelope of Hind's protostar. However, at the very faint light levels characteristic of this portion of the map, slight variations in the thermal background over the time period of the observations could affect the polarization position angles and

amplitudes. Thus, an accurate understanding of the near-infrared polarization structure of the faintest parts of Hind's Nebula probably necessitates observations from space.

4. DISCUSSION

Although the morphology and long-wavelength flux density levels are consistent with the interpretation that the intensity peak in Hind's Nebula is a deeply embedded protostar, it remains possible that this region is only a density enhancement. If so, visible and near-infrared photons from T Tauri would be reflected more effectively and submillimeter photons emitted more abundantly from this region than from less dusty regions of Hind's Nebula, simply because of the density difference. If this interpretation is correct, the temperature and emissivity characteristics of the intensity peak should be indistinguishable from those that characterize the rest of Hind's Nebula. However, in this section, based on calculations that show that the submillimeter emissivity function at the position of the intensity peak is different from that of the larger nebula, we demonstrate that the density enhancement interpretation is unlikely and that the embedded protostar interpretation is quite strong.

4.1. Emission from the Dark Cloud

First, we make model calculations for the large region of background emission that envelops T Tauri and Hind's protostar. The flux from dust grains in a given region of the map is given by the gray body spectrum

$$F_\nu = \Omega_s B(\nu, T)(1 - e^{-\tau_\nu}),$$

where $B(\nu, T)$ is the temperature- and frequency-dependent Planck function and τ_ν is the frequency-dependent optical depth. The optical depth is proportional to the mass density and the dust grain opacity, and the dust grain opacity is assumed to take the form of a power law, $\kappa_\nu = \kappa_0(\nu/\nu_0)^\beta$, where κ_0 is the value of grain opacity ($0.1 \text{ cm}^2 \text{ g}^{-1}$) at frequency ν_0 (1200 GHz; Hildebrand 1983). Thus, our calculations are SED fits with three variables, Ω_s , T , and β ; Ω_s is constrained from our observations. We then impose a range of temperatures to find $\beta(T)$, where T is limited to values appropriate for the environment.

The gas around T Tauri has a kinetic temperature that is roughly 10 K (Edwards & Snell 1982), and the dust temperature is likely to be comparable to the gas temperature (Krügel & Walmsley 1984) or perhaps slightly warmer because of heating by the general interstellar medium radiation field and cosmic rays. We find $\beta(T = 20) = 2.2$ and $\beta(T = 25) = 2.0$, using 450 and 850 μm measurements we have made for the flux from the nebula. Our results are unchanged if we also include the 2.7 mm flux density for the resolved emission observed toward T Tauri by Hogerheijde et al. (1997a). Thus, we conclude that these observations are consistent with an extended cloud characterized by $\beta \simeq 2$ and $T \simeq 20$ –25 K, which are reasonable values for β and T for an externally heated cloud. Such large β indices are characteristic of other clouds and are distinctly different from the β -values near unity that characterize protostars (e.g., Hogerheijde et al. 1997a).

For a given temperature and β , the dust mass of an isothermal, optically thin dust cloud is given by (Hildebrand 1983)

TABLE 3
DUST PROPERTIES

Submillimeter Source	Temperature Range (K)	Beta	M_{dust}^a (M_{\odot})
Dark Cloud	20–25	2.2–2.0	4.0×10^{-3}
Hind's Protostar	20–40	1.3–1.0	$15\text{--}4 \times 10^{-5}$

^a Multiply by 100 to obtain total mass.

$$M_{\text{dust}} = \frac{F_{\nu} D^2}{\kappa_{\nu} B(\nu, T)},$$

where D is the distance to the submillimeter source and $M_{\text{total}} = 100M_{\text{dust}}$, assuming the mass ratio of gas to dust is 100. For the large cloud seen in our SCUBA images, we find $M_{\text{total}} \simeq 0.4 M_{\odot}$ (Table 3). The total mass we have estimated for the extended emission is larger than that reported by Hogerheijde et al. (1997a) for the envelope flux around T Tauri; however, our SCUBA-derived maps enable us to measure the emission from a larger region than was possible in the single pointing, large-aperture data obtained by Hogerheijde et al.

4.2. Hind's Protostar

For the submillimeter intensity peak in Hind's Nebula, we again assume that the emission is from an isothermal dust distribution. We know from the polarimetric maps that very little, if any, visible and near-infrared light emerges directly from the vicinity of Hind's protostar. Thus, since the effective temperature of this region is likely lower than that around T Tauri, we assume a characteristic temperature of 20–40 K; from the geometric mean of the 850 μm measurements, we estimate a source size of $13''.2$. We find $\beta = \sim 1.2$, the submillimeter luminosity is $\sim 10^{-1} L_{\odot}$, and $M_{\text{total}} \sim 10^{-2} M_{\odot}$.

This calculation reveals a β for this intensity peak that is markedly different from the dark cloud material and from the $\beta \simeq 2$ results that characterize dust in larger clouds. The near-unity value of β is also typical of T Tauri and pre-main-sequence stars. These calculations therefore provide good evidence that the peak we have called Hind's protos-

tar is, in fact, an embedded protostellar source. The location of Hind's protostar makes it a primary candidate for the driving source of the Herbig-Haro source located $\sim 15''$ northwest of it (Bührke et al. 1986).

Although for Hind's protostar we are limited to photometric data at only three wavelengths (the polarimetry demonstrated that most or all of the observed K -band flux from the region of Hind's protostar is reflected light from T Tauri), we can make an assessment of the evolutionary stage occupied by Hind's protostar. We have calculated the mean frequency $\langle \nu \rangle$ (Ladd et al. 1991) and bolometric temperature T_{bol} (Myers & Ladd 1993) for Hind's protostar assuming $12.84 < K < 19$. We find $3.4 \times 10^{12} \text{ Hz} \leq \langle \nu \rangle \leq 6.9 \times 10^{13} \text{ Hz}$, $0.16 L_{\odot} \leq L_{\text{bol}} \leq 0.94 L_{\odot}$ and $40 \text{ K} < T_{\text{bol}} < 375 \text{ K}$. This T_{bol} identifies Hind's protostar as a class I young stellar object, with an age a few times 10^5 yr. For comparison, Chen et al. (1995) found $T_{\text{bol}} = 3452 \text{ K}$ (and $L_{\text{bol}} = 12 L_{\odot}$) for T Tauri N and $T_{\text{bol}} = 501 \text{ K}$ (and $L_{\text{bol}} = 15 L_{\odot}$) for T Tauri S.

5. SUMMARY

We have imaged T Tauri and the nearby reflection nebula, Hind's Nebula, at 450 and 850 μm using SCUBA and at K band using COB and have obtained a single photometric observation of Hind's protostar at 1300 μm using SCUBA. The three maps reveal that the nebulosity covers a square arcminute in the vicinity of T Tauri and Hind's Nebula and has two significant intensity peaks, one around T Tauri itself and a second at the southern tip of Hind's Nebula. Calculations of the long-wavelength emissivity demonstrate that the dust emissivity index β is ~ 2 for the large nebula and ~ 1.2 for the intensity peak in Hind's Nebula. This calculation demonstrates that the second peak is, in fact, a bona fide protostar we call Hind's protostar. In thermal emission, the FWHM of the source region around T Tauri is several hundred AU and is oriented at about the same position angle as the smaller, interferometrically resolved source centered on T Tauri N; in reflected light, dust is seen out to several thousand AU. In addition, dust clearly connects the circumstellar nebula immediately around T Tauri to Hind's protostar. This dust, as well as dust throughout all of Hind's Nebula, is detected both in scattered and thermally emitted light.

REFERENCES

- Adams, F. C., Lada, C., & Shu, F. 1988, *ApJ*, 326, 825
Akeson, R. L., Koerner, D. W., & Jensen, E. L. N. 1998, *ApJ*, 505, 358
Beckwith, S. V. W., & Sargent, A. I. 1991, *ApJ*, 381, 250
Bieging, J., Cohen, M., & Schwartz, P. R. 1984, *ApJ*, 282, 699
Bührke, T., Brugel, E. W., & Mundt, R. 1986, *A&A*, 163, 83
Burrows, C. J., et al. 1996, *ApJ*, 473, 437
Chen, H., Myers, P. C., Ladd, E. F., & Wood, D. O. S. 1995, *ApJ*, 445, 377
Cohen, M., Bieging, J., & Schwartz, P. R. 1982, *ApJ*, 255, L103
Edwards, S., & Snell, R. L. 1982, *ApJ*, 261, 151
ESA. 1997, *The Hipparcos and Tycho Catalogues*, ESA SP-1200
Gear, W. K., & Cunningham, C. R. 1995, in *ASP Conf. Ser. 75, Multifield Systems for Radio Telescopes*, ed. D. T. Emerson & J. M. Payne (San Francisco: ASP), 215
Galli, D., & Shu, F. H. 1993, *ApJ*, 417, 220
Hildebrand, R. H. 1983, *QJRAS*, 24, 267
Hodapp, K. 1994, *ApJS*, 94, 615
Hogerheijde, M. R., van Dishoeck, E. F., Blake, G. A., & van Langevelde, H. J. 1997a, *ApJ*, 489, 293
Hogerheijde, M. R., van Langevelde, H. J., Mundy, L. G., Blake, G. A., & van Dishoeck, E. F. 1997b, *ApJ*, 490, L99
Huard, T. C., Weintraub, D. A., & Kastner, J. H. 1997, *MNRAS*, 290, 598
Koerner, D. W., Jensen, E. L. N., Mathieu, R. D., & Ghez, A. M. 1996, *BAAS*, 188.4007
Koerner, D. W., Jensen, E. L. N., Mathieu, R. D., Ghez, A. M., & Cruz, K. L. 1999, in preparation
Koerner, D. W., Sargent, A. I., & Beckwith, S. V. W. 1993, *ApJ*, 408, L93
Krügel, E., & Walmsley, C. M. 1984, *A&A*, 130, 5
Ladd, E. F., Adams, F. C., Casey, S., Davidson, J. A., Fuller, G. A., Harper, D. A., Myers, P. C., & Padman, R. 1991, *ApJ*, 366, 203
Mannings, V., & Emerson, J. P. 1994, *MNRAS*, 267, 361
———. 1997, *ApJ* 490, 792
McCaughrean, M. J., & O'Dell, C. R. 1996, *AJ*, 111, 1977
McCaughrean, M. J., Chen, H., Bally, J., Erickson, E., Thompson, R., Rieke, M., Schneider, G., Stolovy, S., & Young, E. 1998, *ApJ*, 492, L157
Momose, M., Ohasi, N., Kawabe, R., Hayashi, M., & Nakano, T. 1996, *ApJ*, 470, 1001
Myers, P. C., & Ladd, E. F. 1993, *ApJ*, 413, L47
Ohashi, N., Hayashi, M., Kawabe, R., & Ishiguro, M. 1996, *ApJ*, 466, 317
Padgett, D., Brandner, W., Stapelfeldt, K., Koerner, D., Terebey, S., Strom, S., & Kenyon, S. 1998, *BAAS*, 192, 1004
Panagia, N., & Felli, M. 1975, *A&A*, 39, 1
Ray, T. P., Muxlow, T. W. B., Axon, D. J., Brown, A., Corcoran, D., Dyson, J., & Mundt, R. 1997, *Nature* 385, 415
Sandell, G. 1994, *MNRAS*, 271, 75
———. 1997, *SCUBA Mapping Cookbook: A First Step to Proper Map Reduction*, Starlink Document, § 11

- Sargent, A. I., & Beckwith, S. 1987, ApJ, 323, 294
Schwartz, P. R., Simon, T., & Campbell, R. 1986, ApJ, 303, 233
Schwartz, P. R., & Spencer, J. H. 1979, MNRAS, 180, 297
Shu, F., Najita, J., Galli, D., Ostriker, E., & Lizano, S. 1993, in *Protostars and Planets III*, ed. E. H. Levy & J. I. Lunine (Tucson: Univ. Arizona Press), 3
Skinner, S. L., & Brown, A. 1996, AJ, 107, 1461
Spencer, J. H., & Schwartz, P. R. 1974, ApJ, 188, L105
Weintraub, D. A., Kastner, J. H., Zuckerman, B., & Gatley, I. 1992, ApJ, 391, 784
Weintraub, D. A., Masson, C. R., & Zuckerman, B. 1989, ApJ, 344, 915
Weintraub, D. A., Sandell, G., & Duncan, W. D. 1989, ApJ, 340, L69
———. 1990, BAAS, 22, 1265
Wright, A. E., & Barlow, M. J. 1975, MNRAS, 170, 41